ACS APPLIED MATERIALS & INTERFACES

Research Article

www.acsami.org

Raman Reporter-Coupled $Ag_{core}@Au_{shell}$ Nanostars for *in Vivo* Improved Surface Enhanced Raman Scattering Imaging and Near-infrared-Triggered Photothermal Therapy in Breast Cancers

Leyong Zeng,[†,‡] Yuanwei Pan,[†] Shouju Wang,[‡] Xin Wang,[‡] Xinmei Zhao,[†] Wenzhi Ren,[†] Guangming Lu,[*,‡,§] and Aiguo Wu[*,†]

[†]Key Laboratory of Magnetic Materials and Devices & Division of Functional Materials and Nanodevices, Ningbo Institute of Materials Technology and Engineering, Chinese Academy of Sciences, Ningbo 315201, P. R. China

[‡]Department of Medical Imaging, Jinling Hospital, School of Medicine, Nanjing University, Nanjing 210002, P. R. China

[§]State Key Laboratory of Analytical Chemistry for Life Science, School of Chemistry and Chemical Engineering, Nanjing University, Nanjing 210093, P. R. China

Supporting Information

ABSTRACT: Noble-metal nanomaterials were widely investigated as theranostic systems for surface enhanced Raman scattering (SERS) imaging, and also for photothermal therapy (PTT) of cancers. However, it was still a major challenge to explore multifunctional nanoprobes with high performance, high stability, and low toxicity. In this work, Raman reporter (DTTC)-coupled $Ag_{core}@Au_{shell}$ nanostars (Ag@Au-DTTC) were synthesized and investigated for *in vivo* improved SERS imaging and near-infrared (NIR)-triggered PTT of breast cancers. By the two-step coupling of DTTC, the SERS signal was improved obviously, and the cytotoxicity of nanoparticles was also decreased by coating Au nanostars onto Ag nanoparticles. The as-prepared Ag@Au-DTTC nanostars showed high photostability and excellent photothermal performance, in which the photothermal conversion efficiency was up to 79.01% under the irradiation of an 808 nm laser. The *in vitro* and *in vivo* SERS measurements of Ag@Au-DTTC nanostars showed that the many sharp and narrow Raman peaks located at 508, 782, 844, 1135, 1242, 1331, 1464, 1510, and 1580 cm^{-1} could be obviously observed in MCF-7 cells and in MCF-7 tumor-bearing nude mice, compared with that in pure DTTC. In 14-day treatments, the tumor volume of MCF-7 tumor-bearing nude mice injected with Ag@Au-DTTC nanostars and irradiated by an 808 nm laser almost disappeared. This study demonstrated that the as-prepared Ag@Au-DTTC nanostars could be excellent multifunctional agents for improved SERS imaging and NIR-triggered PTT of breast cancers with low risk.

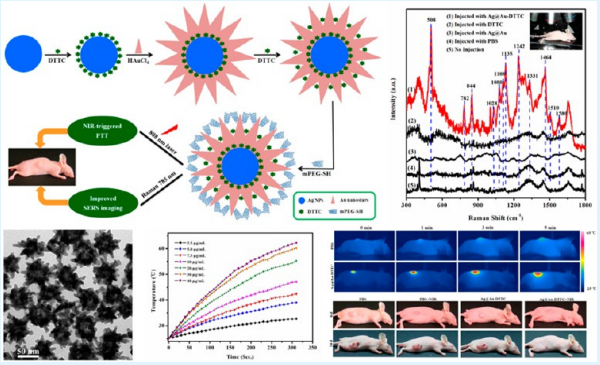

KEYWORDS: *$Ag_{core}@Au_{shell}$ nanostars, improved SERS imaging, Raman reporter, photothermal therapy, 808 nm laser*

1. INTRODUCTION

Malignant tumors have become one of the most serious threats to human beings, and it was very urgent that we develop new techniques to diagnose and treat cancers. In recent years, many efforts have been devoted to the development of nanoprobes with diagnosis and therapy.[1−5] At present, the popular theranostic nanoprobes include magnetic resonance imaging (MRI), computed tomography (CT), positron emission tomography (PET), fluorescent imaging, photoacoustic imaging, surface enhanced Raman scattering (SERS) imaging, and imaging-guided photothermal therapy (PTT), photodynamic therapy (PDT), drug/gene delivery, and so on. In the reported theranostic systems, nanoprobes based on SERS imaging showed important application potentials in clinical trials due to their high sensitivity and anti-interference, and were promising as a new theranostic platform for multimodal imaging and visualizing therapy of cancers.[6,7]

Generally, noble-metal nanomaterials and their alloys played important roles in SERS imaging and SERS-guided therapy of cancers due to enhanced local field and localized surface plasmon resonance (SPR) property. In past decades, spherical gold (Au) or silver (Ag) nanoparticles, Au nanorods, and nanostars were all investigated as SERS-active substrates.[8−12] Moreover, due to good biocompatibility and near-infrared (NIR) absorption, Au nanomaterials were also applied in photoacoustic imaging, CT, PTT, and PDT, besides SERS imaging.[13−21] By coupling Au or Ag nanoparticles with other nanomaterials (such as Au@Pt, Ag-

Received: May 25, 2015
Accepted: July 10, 2015
Published: July 23, 2015

DOI: 10.1021/acsami.5b04548
ACS Appl. Mater. Interfaces 2015, 7, 16781−16791

graphene, Au-graphene-doxorubicin (DOX), Au−Fe_3O_4, Au−Cu alloy, Au-TiO_2-DOX, and so on), the new theranostic systems were also designed for SERS imaging, MRI, CT, antibacteria, PTT, and chemotherapy.[22−28] Although Au, Ag, and their nanocomposites were all used as SERS-active substrates, Ag nanoparticles were still believed to be the best candidate due to a high SERS enhancement factor. Unfortunately, it was known that Ag nanoparticles have poor biocompatibility due to their easy-oxidizability, by which the cytotoxicity and genotoxicity of human cells might be caused,[29−31] and the SERS activity could also greatly decrease. Therefore, exploring high SERS-active substrate materials with low toxicity and high stability was important for the *in vivo* SERS imaging and therapy.

Compared with Ag nanoparticles, Au nanomaterials had good biocompatibility, and showed high SPR effect and NIR absorption. Au−Ag alloy nanomaterials provided another important theranostic platform for SERS imaging and SERS-guided PTT. Recently, Au@Ag core−shell nanoparticles, nanoshuttles, nanotubes, and nanostars were synthesized and investigated for SERS imaging,[32−36] and Ag@Au core−shell nanomaterials were also prepared, in which the Au component was an excellent candidate as a photothermal agent due to strong NIR absorption, such as Ag@Au spherical nanoparticles for SERS, Ag@Au nanourchins for PTT, and hollow Ag@Au nanoshells for chemotherapy and PTT.[37−39] As an important type of Au nanostructures, Au nanostars showed good SERS enhancement performance due to their metal-tip structure and had high photothermal conversion efficiency (~80%) indicating important potential in PTT of cancers.[37] However, it was still a major challenge to combine the high SERS sensitivity of the Ag-based component and the high photothermal conversion efficiency of the Au nanostar component. Thus, there are no reports of $Ag_{core}@Au_{shell}$ nanostars for simultaneous SERS imaging and PTT of cancers. Therefore, by coating Au nanostars onto Ag nanoparticles, the obtained $Ag_{core}@Au_{shell}$ nanostars will possess excellent performance of SERS imaging and PTT with low risk.

In this article, Raman report (DTTC)-coupled $Ag_{core}@Au_{shell}$ (Ag@Au-DTTC) nanostars were synthesized for improved SERS imaging and NIR-triggered high efficient PTT in breast cancers. By coating Au nanostars onto Ag nanoparticles, the cytotoxicity could be decreased, compared with that of bare Ag nanoparticles. By two-step coupling DTTC, the SERS signal of Ag@Au-DTTC was obviously improved both *in vitro* and *in vivo*. Moreover, the as-prepared Ag@Au-DTTC nanostars showed high photostability and photothermal conversion efficiency. Under the irradiation of an 808 nm laser, the *in vitro* and *in vivo* therapies indicated the excellent PTT performance of Ag@Au-DTTC nanostars in breast cancers. This work demonstrates that the as-prepared $Ag_{core}@Au_{shell}$ nanostars could be strong SERS-active substrates for improved SERS imaging and excellent photothermal agents for PTT in breast cancers.

2. EXPERIMENTAL SECTION

2.1. Reagents and Materials. Silver nitrate ($AgNO_3$), potassium iodide (KI), ascorbic acid (AA), and gold(III) chloride hydrate ($HAuCl_4{\cdot}4H_2O$), trisodium citrate dehydrate ($Na_3C_6H_5O_7$), and hydrochloric acid (HCl) were purchased from Sinopharm Chemical Reagent Co. Ltd. (Shanghai, China). Methoxy polyethylene glycol thiol (mPEG-SH, MW = 1000) was purchased from Seebio Biotech Inc. (Shanghai, China). 3,3′-diethylthiatricarbocyanine iodide (DTTC iodide), 5-diphenyl-2-*H*-tetrazolium bromide (MTT), Dulbecco's modified Eagle's medium (DMEM), and fetal bovine serum (FBS, Gibco) were purchased from Keygen Biotech Co. Ltd. (Nanjing, China). Calcein acetoxymethyl ester (CAM) and ethidium homodimer-1 (EthD-1) were purchased from life technologies (Shanghai, China). All of the chemicals were used as received without further purification.

2.2. Synthesis of Ag@Au-DTTC Nanostars. Ag nanoparticles with a diameter of about 20−30 nm were synthesized following the previously reported method.[40] Briefly, 50 μL of AA aqueous solution with a concentration of 0.1 mM was added into 47.5 mL of boiling deionized water and boiled for another 1 min. Subsequently, the mixed solutions (1 mL of 1 wt % $Na_3C_6H_5O_7$, 0.25 mL of 1 wt % $AgNO_3$, and 50 μL of 0.06 mM KI were consecutively added into 1.25 mL of deionized water under stirring at room temperature, and the stirring was maintained for 5 min) were added into the above AA solution. After they were boiled for another 1 h, the as-prepared Ag nanoparticles were collected by centrifugation and washed in water three times and were redispersed in 50 mL of deionized water.

Ag@Au-DTTC nanostars were synthesized by two-step coupling DTTC (1#: Ag@Au-DTTC). Briefly, 0.75 mL of the as-prepared Ag nanoparticles were added into 9 mL of deionized water under stirring, and 50 μL of 0.1 mM DTTC was added dropwise to form Ag-DTTC nanoparticles. After 10 min, 7.5 μL of 0.1 M HCl and 1 mL of 2.5 mM $HAuCl_4$ aqueous solutions were consecutively added, and 60 μL of 10 mM $AgNO_3$ and 50 μL of 100 mM AA were simultaneously added into the above solution under vigorous stirring. After 30 s, 150 μL of 0.1 mM DTTC was dropped into the as-prepared nanoparticles for the second time, and the stirring was maintained for another 10 min. As a comparison, Ag@Au-DTTC nanostars were also synthesized by one-step coupling DTTC (2#: Ag@Au-DTTC). Briefly, Ag@Au nanostars were first synthesized, and then 200 μL of 0.1 mM DTTC was dropped into the as-prepared Ag@Au nanostars, and the stirring was maintained for another 10 min. In the growth of Au nanostars, adding $AgNO_3$ was responsible for the yield and shape of anisotropic Au nanostars, in which the underpotential deposition of Ag^+ on certain crystal facets of Ag seeds led to the formation of multiple branches by blocking certain facets.[46,48]

Finally, the as-prepared Ag@Au-DTTC nanostars were modified with mPEG-SH. Briefly, 20 μL of 2 mM mPEG-SH in aqueous solution was added into the as-prepared Ag@Au-DTTC nanostars under stirring. After 30 min, the mPEG-SH-modified Ag@Au-DTTC nanostars were collected by centrifugation and washed in water three times, and were redispersed in 10 mL of deionized water.

2.3. Characterization. The transmission electron microscopy (TEM) images, scanning transmission electron microscopy (STEM), and energy dispersed X-ray spectra (EDS) were characterized by a Tecnai F20 transmission electron microscope operated at 200 kV. The dynamic light scattering (DLS) spectra were characterized by a Brookhaven ZetaPALS Analyzer. The UV−vis absorption spectra were characterized by PerkinElmer Lambda 35 UV−vis spectrophotometer. The SERS spectra were measured by a Renishaw inVia Raman spectrometer. The cell viabilities in the MTT assay were measured by a BioTek ELX 800 microplate reader. The hematoxylin and eosin (H&E) staining were examined by a Leica DMI 3000 optical microscope.

2.4. Photothermal Performance and Photostability Studies. The photothermal performance of Ag@Au-DTTC nanostars was investigated using an 808 nm laser and an infrared (IR) thermal imaging system under different conditions. An IR thermal imaging system (MAG-V30, Vst Light & Technology Ltd., Wuhan of China) was employed for the recording temperature change. The temperature value was recorded once every 10 s, and simultaneously, the thermal imaging was mapped. (1) Changing the power density of the 808 nm laser: 2 mL of Ag@Au-DTTC nanostars (40 μg/mL) was irradiated by an 808 nm laser for 5 min, in which the power density of the 808 nm laser was 0.4, 0.8, 1.2, 1.6, 2.0, 2.4, and 3.0 W/cm^2. (2) Changing the concentration of Ag@Au-DTTC nanostars: 2 mL of Ag@Au-DTTC nanostars was irradiated by an 808 nm laser (2.0 W/cm^2) for 5 min, in which the concentration of Ag@Au-DTTC nanostars was 2.5, 5.0, 7.5, 10, 20, 30, and 40 μg/mL. (3) Changing the irradiation time of a 808 nm laser: 2 mL of Ag@Au-DTTC nanostars (40 μg/mL) was irradiated by an 808 nm laser (2.0 W/cm^2) for different times of 5, 10, 15, 20, 25, and 30 min. The temperature variation and thermal imaging were monitored by an IR thermal imaging system, and the changes of UV−vis absorption and

DOI: 10.1021/acsami.5b04548
ACS Appl. Mater. Interfaces 2015, 7, 16781−16791

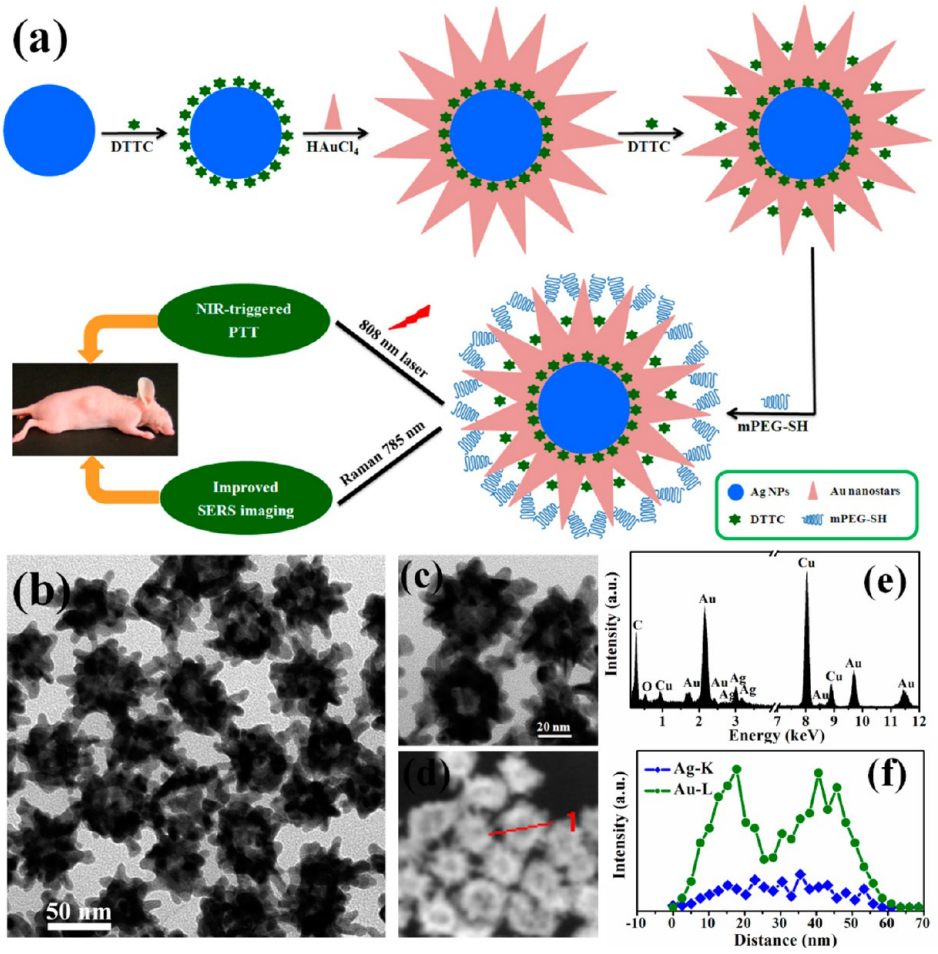

Figure 1. Synthesis and characterization of Ag@Au-DTTC nanostars. (a) Scheme of Ag@Au-DTTC nanostars for *in vivo* improved SERS imaging and NIR-triggered PTT of breast cancers; (b) TEM images of Ag@Au-DTTC nanostars; (c and e) localized TEM images and the corresponding EDS spectrum in dot scanning of Ag@Au-DTTC nanostars; (d and f) localized STEM images and the corresponding EDS spectrum in line scanning of Ag@Au-DTTC nanostars.

size of Ag@Au-DTTC nanostars irradiated by an 808 nm laser with different times were also measured by UV−vis absorption spectra and DLS. Moreover, the photostability of Ag@Au-DTTC nanostars was also investigated under the irradiation of an 808 nm laser every other 5 min over 10 on/off cycles.

2.5. Cell Culture and Cytotoxicity Assay. Human breast cancer cells (MCF-7) were cultured in DMEM culture medium supplemented with 10% of FBS, 100 units/mL of penicillin, and 100 mg/mL of streptomycin at 37 °C in 5% CO_2. Briefly, MCF-7 cells in logarithmic growth were cultured in 96-well plates for 24 h and then incubated with Ag nanoparticles and Ag@Au-DTTC nanostars for another 24 h. The concentrations were 0, 1, 2, 3, 4 μg/mL for Ag nanoparticles, and 0, 10, 20, 30, 40 μg/mL for Ag@Au-DTTC nanostars, in which the Ag concentration was equivalent (the addition of Ag nanoparticles during the synthesis of Ag@Au-DTTC nanostars was considered to calculate Ag concentration in the sample of Ag@Au-DTTC nanostars, not considering the addition of the $AgNO_3$ agent). Finally, the cell viabilities were measured by an MTT assay.

2.6. *In Vitro* PTT Studies. MCF-7 cells in logarithmic growth were cultured in 96-well plates for 24 h and then incubated with Ag@Au-DTTC nanostars for another 24 h by irradiating an 808 nm laser under different conditions. (1) MCF-7 cells incubated with Ag@Au-DTTC nanostars (40 μg/mL) were irradiated by an 808 nm laser for 5 min, in which the power density was 0, 0.4, 0.8, 1.2, 1.6, and 2.0 W/cm^2. (2) MCF-7 cells incubated with Ag@Au-DTTC nanostars (40 μg/mL) were irradiated by an 808 nm laser (2.0 W/cm^2), in which the irradiation time was 0, 1, 2, 3, 4, and 5 min. (3) MCF-7 cells incubated with Ag@Au-DTTC nanostars were irradiated by an 808 nm laser (2.0 W/cm^2) for 5 min, in which the concentrations of Ag@Au-DTTC nanostars were 0, 10, 20, 30, and 40 μg/mL. Alternatively, MCF-7 cells in the control were also irradiated by an 808 nm laser with different power densities and different times. Finally, the viabilities of MCF-7 cells were measured by an MTT assay. Furthermore, the viabilities of MCF-7 cells in the control and incubated with Ag@Au-DTTC nanostars (40 μg/mL) under the irradiation of an 808 nm laser (2.0 W/cm^2) for 0, 1, 3, and 5 min were also characterized by CAM/EthD-1 staining, in which live/dead cells could be directly observed in green/red.

2.7. *In Vitro* SERS Imaging. Raman spectra of different nanoparticles and cells incubated with nanoparticles were measured by a Raman spectrometer with the laser wavelength of 785 nm. For Raman spectra of nanoparticles, 1 mL of pure DTTC (1 μM), Ag@Au (40 μg/mL), and Ag@Au-DTTC (40 μg/mL) nanostars was dispersed in PBS, and their Raman spectra were measured with a wavelength of 785 nm (the laser power was 14 mW, and the intergration time was 10 s). For Raman spectra of cells, MCF-7 cells in logarithmic growth were cultured in 35 mm culture dishes for 24 h and then incubated with pure DTTC (1 μM in PBS), Ag@Au (40 μg/mL in PBS), and Ag@Au-DTTC (40 μg/mL in PBS) nanostars for another 4 h. Finally, the cells were washed with PBS three times, mixed with paraformaldehyde, and the Raman spectra were measured at the different sites of cytoplasm and nucleus with a wavelength of 785 nm (the laser power was 140 mW, and the intergration time was 10 s).

2.8. Animal Models and *in Vivo* Biocompatibility. Female Balb/c (nu/nu) nude mice (18−20 g, 4−6 weeks old) were used in this work. All of the experimental protocols involving animals were approved by the Institutional Animal Care and Use Committee of Jinling Hospital,

DOI: 10.1021/acsami.5b04548
ACS Appl. Mater. Interfaces 2015, 7, 16781−16791

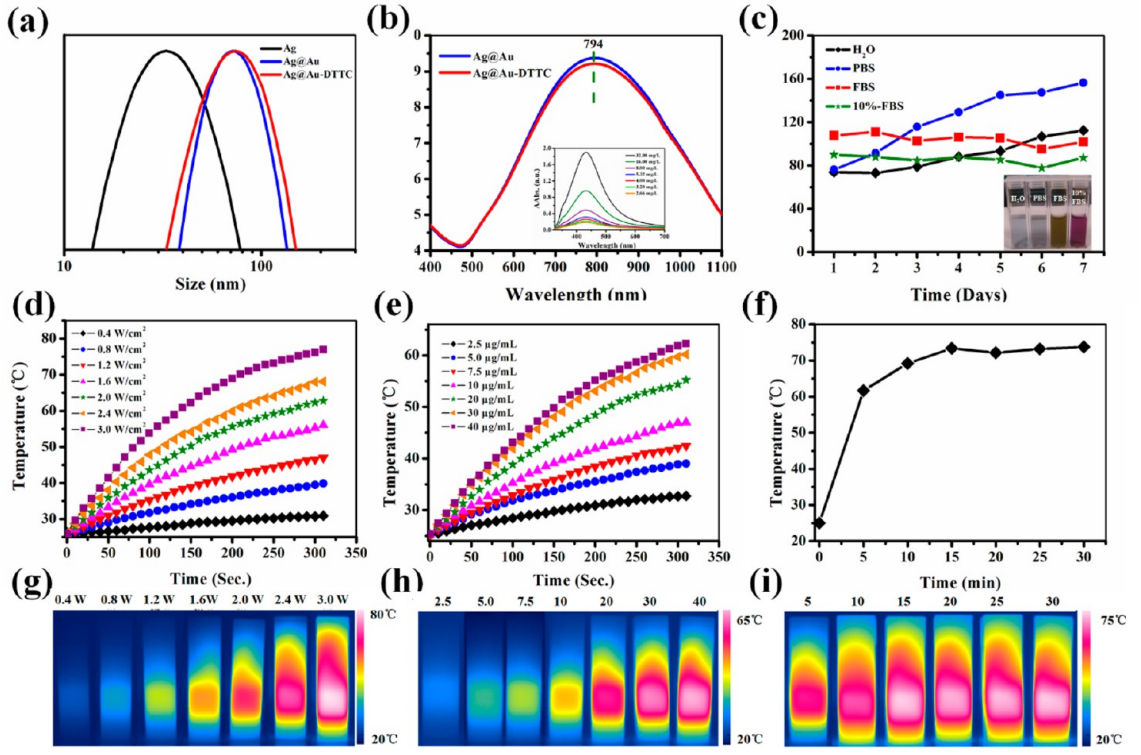

Figure 2. Size distribution, UV−vis absorption spectra of nanoparticles, and temperature variation and the corresponded IR thermal imaging of Ag@Au-DTTC nanostars by irradiating with 808 nm laser under different conditions. (a) DLS curves of Ag, Ag@Au, and Ag@Au-DTTC nanostars; (b) UV−vis absorption spectra of Ag, Ag@Au, and Ag@Au-DTTC nanostars (the inset shows the UV−vis absorption spectra of Ag nanoparticles under different concentrations); and (c) the size change of Ag@Au-DTTC nanostars dispersed in water, PBS buffer, FBS, and 10% FBS between 7 days by DLS characterization. (d and g) The concentration of nanoparticles was 40 μg/mL, the irradiation time of 808 nm laser was 5 min, and the power density was changed from 0.4, 0.8, 1.2, 1.6, 2.0, 2.4, to 3.0 W/cm^2; (e and h) The power density of the 808 nm laser was 2.0 W/cm^2, the irradiation time was 5 min, and the concentration of nanoparticles was changed form 2.5, 5.0, 7.5, 10, 20, 30, to 40 μg/mL; (f and i) The concentration of nanoparticles was 40 μg/mL, the power density of the 808 nm laser was 2.0 W/cm^2, and the irradiation time was changed from 5, 10, 15, 20, 25, to 30 min.

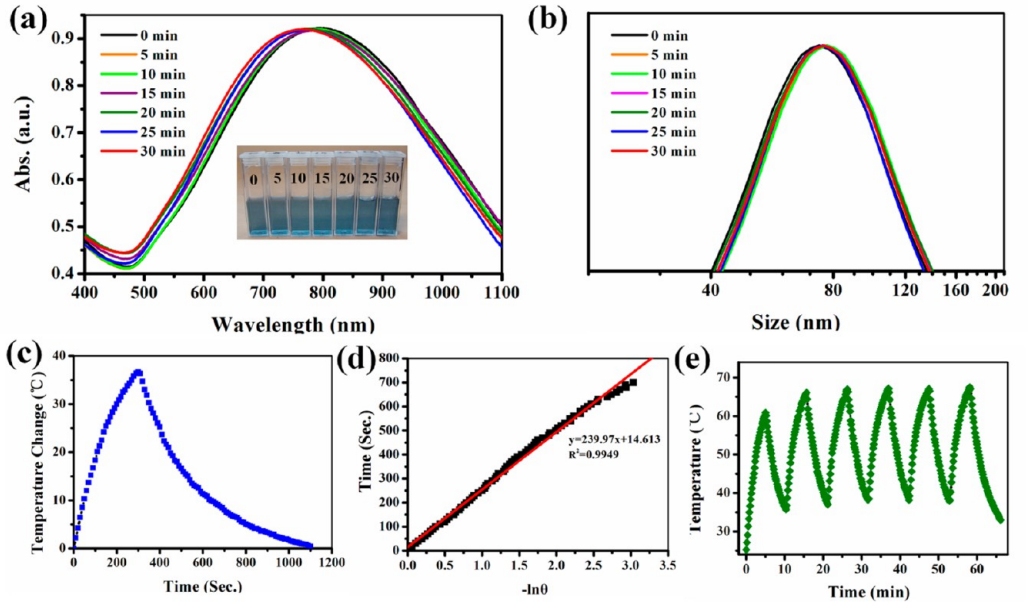

Figure 3. UV−vis absorption spectra, DLS curves, photothermal conversion efficiency, and photothermal stability of Ag@Au-DTTC nanostars (40 μg/mL) under the irradiation of an 808 nm laser (2W/cm^2) with different times from 0, 5, 10, 15, 20, 25, to 30 min. (a) UV−vis-NIR absorption spectra of Ag@Au-DTTC nanostars, and real photographs of nanoparticle colloids in the inset; (b) DLS curves of Ag@Au-DTTC nanostars. (c) The temperature variation of Ag@Au-DTTC nanostars was irradiated by an 808 nm laser for 300 s, and then the laser was shut off; (d) The linear relationship of time data versus −ln θ obtained from the cooling period of panel c; (e) the temperature variation of Ag@Au-DTTC nanostars over 10 on/off cycles of 808 nm laser irradiation.

DOI: 10.1021/acsami.5b04548
ACS Appl. Mater. Interfaces 2015, 7, 16781−16791

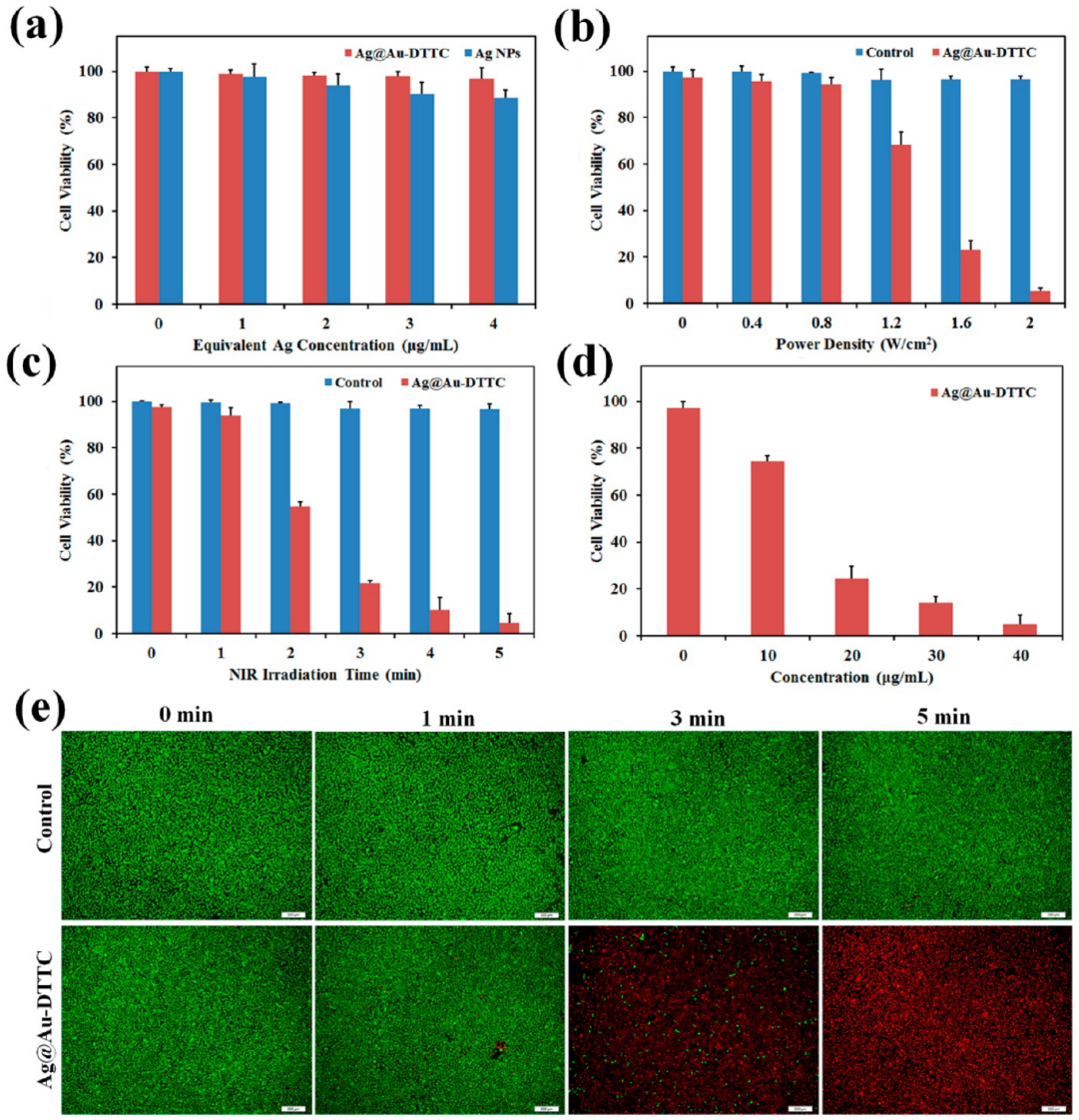

Figure 4. *In vitro* viabilities of MCF-7 cells under different conditions characterized by the MTT assay and live/dead cell staining. (a) Cytotoxicity of MCF-7 cells incubated with Ag nanoparticles and Ag@Au-DTTC nanostars, in which the Ag concentration was equivalent. (b) Viabilities of MCF-7 cells in the control and incubated with Ag@Au-DTTC nanostars under the irradiation of an 808 nm laser with different power densities, in which the concentration of nanoparticles was 40 μg/mL, and the irradiation time was 5 min. (c) Viabilities of MCF-7 cells in the control and incubated with Ag@Au-DTTC nanostars under the irradiation of an 808 nm laser with different irradiation times, in which the concentration of nanoparticles was 40 μg/mL, and the power density was 2W/cm^2. (d) Viabilities of MCF-7 cells incubated with Ag@Au-DTTC nanostars with different concentrations under the irradiation of an 808 nm laser, in which the power density was 2W/cm^2, and the irradiation time was 5 min. (e) Viabilities of MCF-7 cells in the control and incubated with Ag@Au-DTTC nanostars under the irradiation of an 808 nm laser with different irradiation times for 0, 1,3, and 5 min by live/dead cell staining.

and all the mice received humane care in compliance with the guide for the Care and Use of Laboratory Animals. Moreover, the experiments in the present study were performed in the Animal Centre of Jinling Hospital. For biocompatibility measurements, 18−20 g of healthy nude mice (4−6 weeks old) were injected with 100 μL of PBS and Ag@Au-DTTC nanostars (200 μg/mL in PBS) via the tail vein. After 14 days, they were sacrificed, and the main organs, the heart, liver, spleen, lung, kidney, and intestine, were dissected for H&E staining. In this work, the tumor model of MCF-7 was established and used. Briefly, MCF-7 cells were diluted with PBS and then injected subcutaneously into each mouse at the back with about 1×10^7 cells. When the tumors grew to be about 50−100 mm^3, the *in vivo* therapy was carried out.

2.9. *In Vivo* SERS Imaging. MCF-7 tumor-bearing nude mice were injected with 100 μL of PBS, pure DTTC (1 μM in PBS), Ag@Au (40 μg/mL in PBS), and Ag@Au-DTTC (40 μg/mL in PBS) nanostars. After 30 min, the Raman spectra of mice were measured with a wavelength of 785 nm (the laser power was 140 mW, and the intergration time was 10 s). As a comparison, the Raman spectrum of a mouse without the injection was also measured at the same conditions.

2.10. *In Vivo* PTT. MCF-7 tumor-bearing nude mice were randomly divided into 4 groups (n = 6, per group) and injected with 100 μL of PBS, PBS + NIR, Ag@Au-DTTC nanostars (40 μg/mL in PBS), and Ag@Au-DTTC nanostars + NIR (40 μg/mL in PBS) for groups of 1, 2, 3, and 4, respectively. Especially, the mice in groups of 2 and 4 were irradiated by an 808 nm laser (2 W/cm^2) for 5 min after 30 min postinjection. The tumor volume and body weight were measured every other day, and the volume was calculated to be length·width·width/2. On the 14th day, the mice were sacrificed, and the tumors and the main organs, heart, liver, spleen, lung, and kidney, were dissected for H&E staining.

2.11. Statistical Analysis. Data were expressed as the mean ± standard deviation. Statistical differences were analyzed by the Student's t test. A value of $p < 0.05$ was taken as statistically significant.

DOI: 10.1021/acsami.5b04548
ACS Appl. Mater. Interfaces 2015, 7, 16781−16791

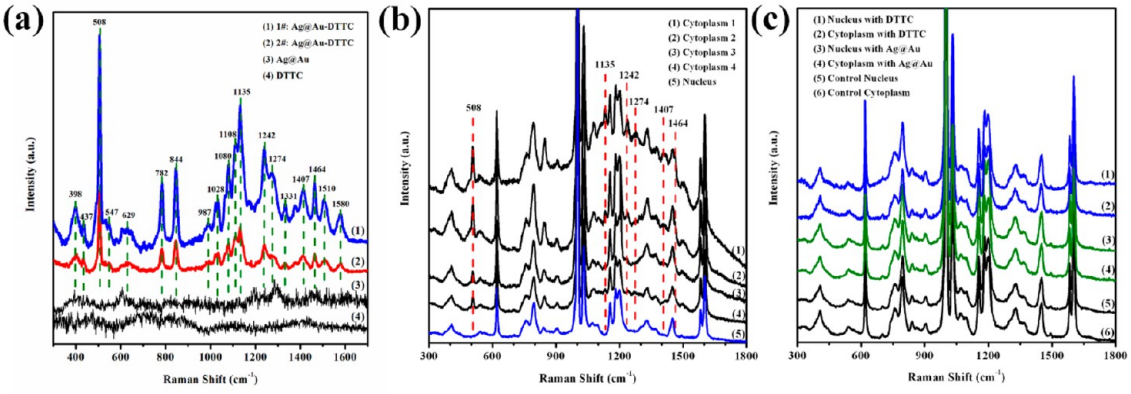

Figure 5. *In vitro* SERS spectra of nanoparticles and MCF-7 cells in the control and incubated with nanoparticles under the excitation of a 785 nm laser. (a) SERS spectra of pure DTTC, Ag@Au, and different Ag@Au-DTTC nanostars (14 mW, 10 s). (b) SERS spectra of MCF-7 cells incubated with Ag@Au-DTTC nanostars at different locations of the cytoplasm and nucleus (140 mW, 10 s). (c) SERS spectra of MCF-7 cells in the control and incubated with pure DTTC and Ag@Au nanoparticles at different locations of the cytoplasm and nucleus (140 mW, 10 s).

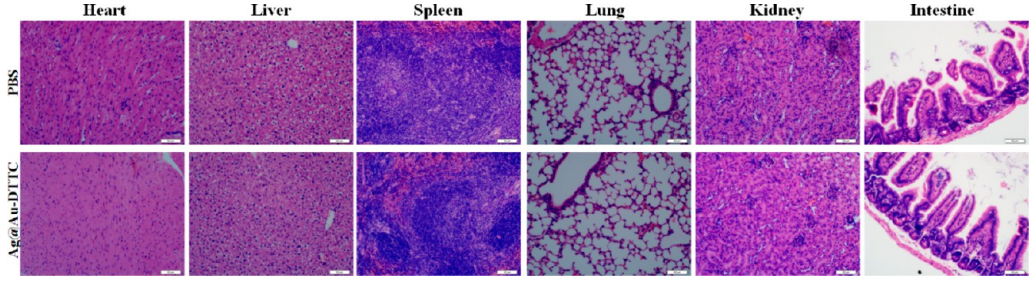

Figure 6. H&E staining images of main organs (heart, liver, spleen, lung, kidney, and intestine) of healthy nude mice injected with PBS buffer and Ag@Au-DTTC nanostars.

3. RESULTS AND DISCUSSION

3.1. Synthesis and Characterization of Ag@Au-DTTC Nanostars. Figure 1a gave schematics of Ag@Au-DTTC nanostars for *in vivo* improved SERS imaging and NIR-triggered PTT in breast cancers. At first, Ag nanoparticles were synthesized and coupled with DTTC for the first time. The TEM image of Ag nanoparticles was shown in Figure S1 (Supporting Information). Then, gold nanostars were grown on the surface of Ag nanoparticles to form Ag@Au core−shell structures and then coupled with DTTC for the second time to form Ag@Au-DTTC nanostars. Finally, mPEG-SH was modified on the surface of Ag@Au-DTTC nanostars for improved SERS imaging and NIR-triggered PTT in breast cancers.

The size distribution and UV−vis absorption spectra of Ag, Ag@Au, and Ag@Au-DTTC nanostars were measured by a DLS and UV−vis spectrometer. As shown in Figure 2a, the size of Ag, Ag@Au, and Ag@Au-DTTC nanostars was about 32, 72, and 74 nm, respectively, which suggested the good dispersibility of Ag@Au-DTTC nanostars. In Figure 2b, the wide absorption bands of Ag@Au and Ag@Au-DTTC nanostars were from 500 to 1100 nm, and the center was located at about 794 nm, which also indicated that DTTC modification will not change the shape and size of Ag@Au nanostars. In order to investigate the performance of SERS imaging and PTT, the stability of mPEG-SH-modified Ag@Au-DTTC nanostars in different media of deionized water, PBS, FBS, and 10% FBS was first characterized by DLS during 7 days. As shown in Figure 2c, the size of Ag@Au-DTTC nanostars was almost constant in FBS and 10% FBS, and slightly bigger in deionized water and in PBS. The results indicated the stability of the as-prepared mPEG-SH-modified Ag@Au-DTTC nanostars in different media, and their stability could be further optimized by adjusting the modification quantity of mPEG-SH molecules.

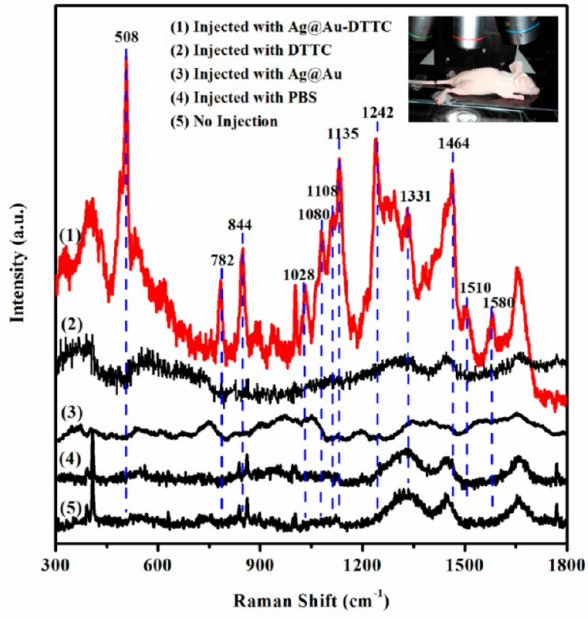

Figure 7. *In vivo* SERS spectra of MCF-7 tumor-bearing nude mice in the control and injected with PBS buffer, Ag@Au, pure DTTC, and Ag@Au-DTTC nanostars under the excitation of a 785 nm laser (140 mW, 10 s).

DOI: 10.1021/acsami.5b04548
ACS Appl. Mater. Interfaces 2015, 7, 16781−16791

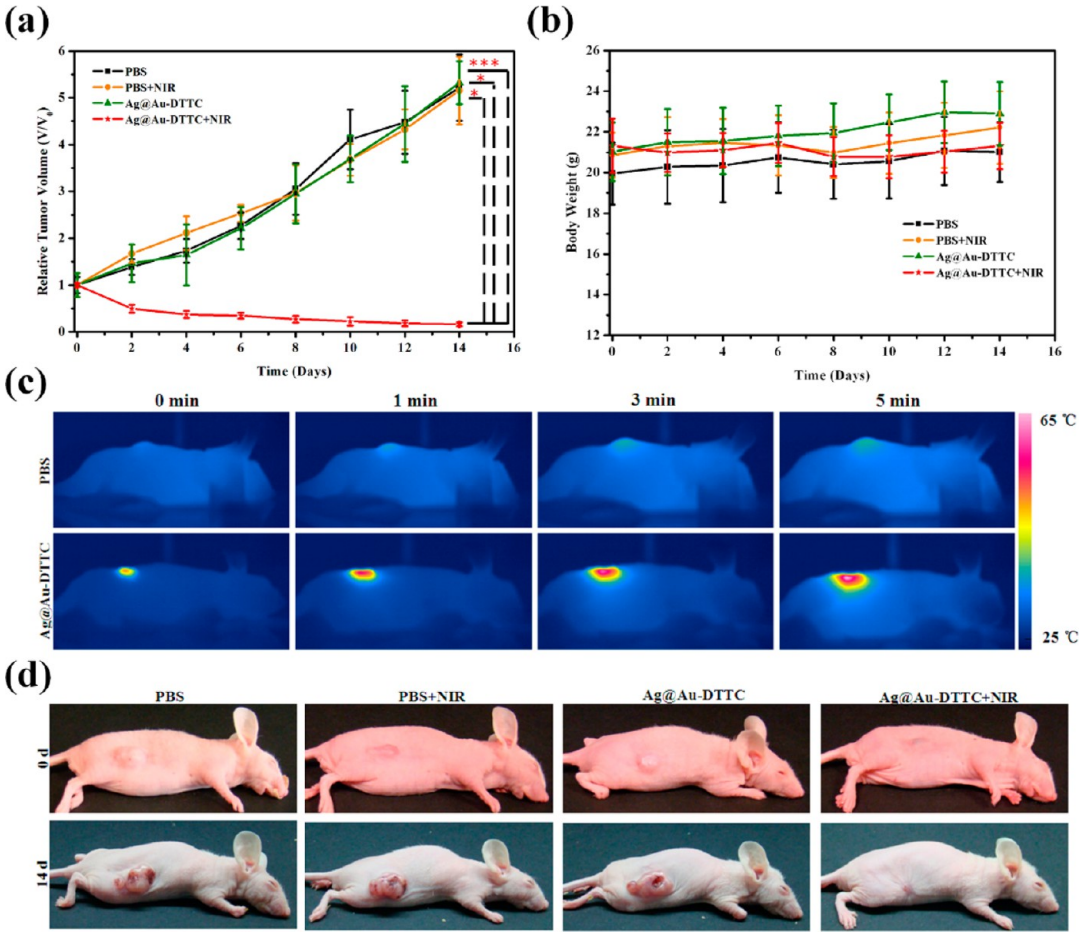

Figure 8. *In vivo* PTT characterization of MCF-7 tumor-bearing nude mice injected with PBS, PBS + NIR irradiation, Ag@Au-DTTC, and Ag@Au-DTTC + NIR irradiation ($n = 6$, per group). (a) The change of relative tumor volume in different groups of PBS, PBS + NIR, Ag@Au-DTTC, and Ag@Au-DTTC + NIR. (b) The change of body weight in different groups of PBS, PBS + NIR, Ag@Au-DTTC, and Ag@Au-DTTC+NIR. (c) The IR thermal imaging of tumor-bearing nude mice injected with PBS and Ag@Au-DTTC under the irradiation of an 808 nm laser for 0, 1, 3, and 5 min. (d) The real photographs of tumor-bearing nude mice in different groups, at the beginning and at the end of 14-day treatments.

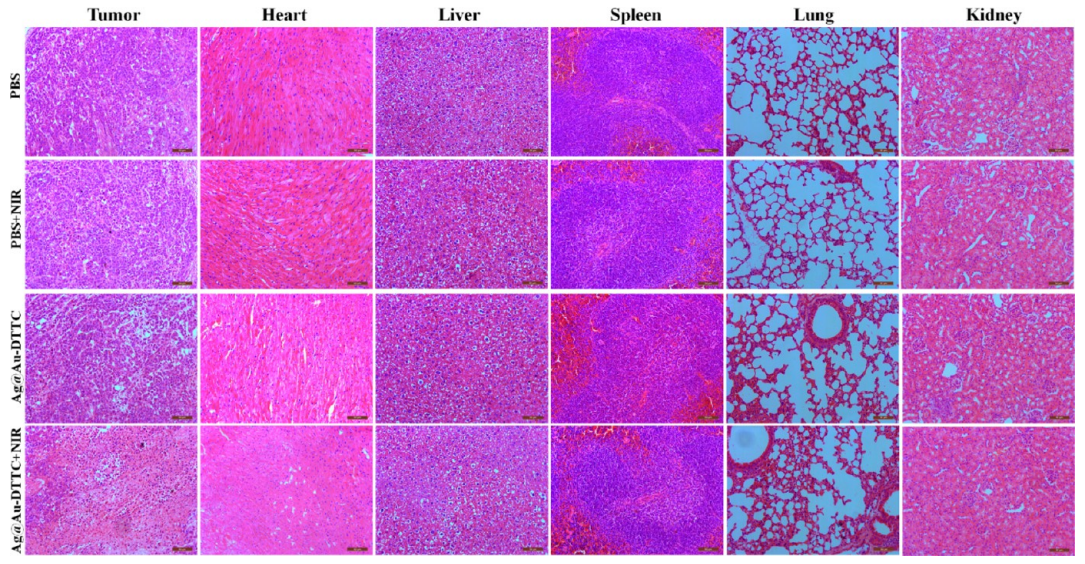

Figure 9. H&E staining images of tumors and main organs (heart, liver, spleen, lung, and kidney) of tumor-bearing nude mice in groups of PBS, PBS + NIR, Ag@Au-DTTC, and Ag@Au-DTTC + NIR.

Using an 808 nm laser and an IR thermal imaging system, the photothermal performance of Ag@Au-DTTC nanostars was investigated, as shown in Figure 2d–i. By increasing the power density of the 808 nm laser from 0.4 to 3.0 W/cm^2 in 5 min, the

DOI: 10.1021/acsami.5b04548
ACS Appl. Mater. Interfaces 2015, 7, 16781–16791

temperature of Ag@Au-DTTC nanostars (40 μg/mL) could increase from 25.50 to 62.75 °C at 2.0 W/cm^2, and to 76.89 °C at 3.0 W/cm^2, respectively, as shown in Figure 2d. Moreover, by fixing the power density of the 808 nm laser in 2.0 W/cm^2, the temperature of Ag@Au-DTTC nanostars could gradually increase by adding the nanoparticle concentration from 2.5 to 40 μg/mL. Especially, when the concentration was higher than 20 μg/mL, the temperature could increase obviously to more than 55 °C in 5 min, as shown in Figure 2e. By increasing the irradiation time of the 808 nm laser from 5 to 30 min, the temperature of Ag@Au-DTTC nanostars (40 μg/mL) could only increase by about 11 °C, as shown in Figure 2f. Furthermore, the real images of IR thermal imaging under different conditions were also shown in Figure 2g to i, which were consistent with the temperature curves in Figure 2d to f.

3.2. Photostability and Photothermal Conversion Efficiency. In order to improve the applicability in clinical settings, the stability of Ag@Au-DTTC nanostars irradiated by an 808 nm laser with different times was investigated using UV−vis absorption spectra and DLS, as shown in Figure 3a and b. When the irradiation time was increased from 0 to 30 min, the peak intensity of UV−vis absorption did not obviously decrease except by a slight blue-shift, and the color of the nanoparticle colloid did also not change. Moreover, the size of nanoparticles did not obviously increase or decrease. The slight blue-shift and size change of Ag@Au-DTTC nanostars could be attributed to the spikes decrease of nanostars after laser irradiation, which could be observed in the TEM image, as shown in Figure S2 (Supporting Information). The results suggested that the as-prepared Ag@Au-DTTC nanostars had good photostability under irradiation of an 808 nm laser.

Photothermal conversion efficiency and photothermal stability played important roles in improving the PTT efficacy of photothermal agents. Figure 3c and d gave the heating−cooling curve and the corresponded fitting curve following the data in the cooling stage of Ag@Au-DTTC nanostars, by irradiating an 808 nm laser for 5 min. According to Figure 3d and the calculation method described in previous reports,[41,42] the photothermal conversion efficiency (η) could be calculated to be 79.01%, which was much higher than that of gold nanorods, nanocages, Cu-based semiconductor nanoparticles, and other polymer photothermal agents.[41−45] Further, the photothermal stability of Ag@Au-DTTC nanostars (40 μg/mL) was characterized by irradiating an 808 nm laser (2W/cm^2) every other 5 min over 10 on/off cycles. As observed in Figure 3e, the temperature variation of Ag@Au-DTTC nanostars was almost constant during 10 on/off cycles of the laser. Therefore, the excellent photothermal conversion efficiency and photothermal stability indicated that the as-prepared Ag@Au-DTTC nanostars had important potential in PTT of cancers.

3.3. Cytotoxicity Assay and *in Vitro* PTT. To assess the application of Ag@Au-DTTC nanostars in biomedicine, the cytotoxicity and *in vitro* PTT performance were measured by MTT assay. Figure 4a showed the viabilities of MCF-7 cells incubated with Ag nanoparticles and Ag@Au-DTTC nanostars for 24 h, in which the Ag concentration was equivalent. Compared with the cell viability of pure Ag nanoparticles of about 88.8%, Ag@Au-DTTC nanostars showed a lower cytotoxicity of about 97.0%, which indicated that the coating of Au nanostars decreased the toxicity of Ag nanoparticles. Figure 4b gave the viabilities of MCF-7 cells in the control and incubated with Ag@Au-DTTC nanostars (40 μg/mL) under irradiation of an 808 nm laser with different power densities for 5 min. A single 808 nm laser was not harmful for MCF-7 cells in the control, but the MCF-7 cells incubated with Ag@Au-DTTC nanostars could be obviously killed under the irradiation of an 808 nm laser, in which the viability of cells could decrease to 68.4%, 23.0%, and 5.2% with the power density of 1.2, 1.6, and 2.0 W/cm^2, respectively. By changing the irradiation time of the 808 nm laser, the viabilities of MCF-7 cells in the control and incubated with Ag@Au-DTTC nanostars (40 μg/mL) were also measured, as shown in Figure 4c. Similarly to Figure 4b, the viability of MCF-7 cells in the control hardly decreased, but the viability of MCF-7 cells incubated with Ag@Au-DTTC nanostars could decrease to 54.7%, 21.8%, 10.3%, and 5.2% with the irradiation time from 2 to 5 min, respectively. Furthermore, under the irradiation of an 808 nm laser with the power density of 2.0 W/cm^2 for 5 min, the viabilities of MCF-7 cells were measured to be 74.6%, 24.5%, 14.1%, and 5.0%, when the concentration of Ag@Au-DTTC nanostars increased from 10 to 40 μg/mL, as shown in Figure 4d. The *in vitro* MTT results suggested that the coating of Au nanotars decreased the cytotoxicity of pure Ag nanoparticles and that Ag@Au-DTTC nanostars could be potential photothermal agents for PTT under the irradiation of an 808 nm laser.

By live/dead cell staining, the *in vitro* PTT performance of MCF-7 cells incubated with Ag@Au-DTTC nanostars (40 μg/mL) was characterized under the irradiation of an 808 nm laser with a power density of 2 W/cm^2, in which the live/dead cells were shown in green/red color, respectively. As shown in Figure 4e, the MCF-7 cells incubated with Ag@Au-DTTC nanostars were hardly killed after 1 min but almost entirely killed after 3 and 5 min. By contrast, the MCF-7 cells in the control were not killed under the irradiation of an 808 nm laser for 1, 3, and 5 min. The staining results were also consistent with that of the MTT assay.

3.4. *In Vitro* SERS Measurement of Ag@Au-DTTC Nanostars. The SERS effect of Ag@Au-DTTC nanostars was assessed by measuring the Raman spectra of different nanoparticles and cells. Figure 5a showed the Raman spectra of pure DTTC, Ag@Au, and Ag@Au-DTTC nanostars, in which Ag@Au-DTTC nanostars were synthesized by the two-step coupling (1#: Ag@Au-DTTC) and one-step coupling (2#: Ag@Au-DTTC) DTTC described in Experimental Section. In Raman spectra of pure DTTC and Ag@Au nanoparticles, no obvious Raman peak was observed other than some broad packages. However, in Raman spectra of Ag@Au-DTTC nanostars, some sharp and narrow peaks were observed at a wavenumber of 398, 508, 782, 844, 1135, 1242, 1331, 1407, 1464, 1510, and 1580 cm^{-1}, and so on, which was clearly distinguished from pure DTTC and Ag@Au nanostars.[23,49] Especially, the SERS enhancement of Ag@Au-DTTC nanostars by two-step coupling DTTC was 2.63 times larger than one-step coupling DTTC, which could be attributed to the combination of Ag and Au substrates. Although only 50 μL of DTTC was added to modify Ag nanoparticles, the SERS intensity could increase rapidly 2.63 times due to the strong SERS enhancement of the Ag-active substrate. Therefore, it could be said that the Ag-active substrate in Ag@Au with twice-modified DTTC played an important role in SERS enhancement, besides the quantity of DTTC. The finding demonstrated that the as-prepared Ag@Au-DTTC nanostars could have potential application as an improved SERS-active imaging probe.

The *in vitro* SERS spectra were also measured by incubating Ag@Au-DTTC nanostars with MCF-7 cells for 4 h. Figure 5b showed the Raman spectra of MCF-7 cells located at different sites of the cytoplasm and nucleus. Compared with the Raman spectrum of the nucleus, the characteristic peaks of DTTC could

DOI: 10.1021/acsami.5b04548
ACS Appl. Mater. Interfaces 2015, 7, 16781−16791

be observed in Raman spectra of cytoplasm with four different sites, which were located at about 398, 508, 1135, 1242, 1274, 1407, and 1464 cm^{-1} and corresponded to the Raman peaks of Ag@Au-DTTC nanostars shown in Figure 5a. Furthermore, the Raman spectra of MCF-7 cells in the control and incubated with pure DTTC and Ag@Au nanoparticles were also measured. As shown in Figure 5c, the Raman peaks of cells incubated with pure DTTC and Ag@Au nanoparticles were the same as that of cells in the control, which indicated that the characteristic peaks of DTTC were not observed in both the cytoplasm and nucleus. Furthermore, the SERS mapping of MCF-7 cells incubated with Ag@Au-DTTC nanostars was also characterized following the Raman intensity located at about 508 cm^{-1}, which was shown in Figure S8a and b (Supporting Information).

3.5. *In Vivo* Biocompatibility and SERS Measurements.

In order to clarify the possible application of Ag@Au-DTTC nanostars in biomedicine, the *in vivo* biocompatibility was investigated by injecting PBS and Ag@Au-DTTC nanostars in healthy nude mice via the tail vein, and then the tissue sections of main organs (heart, liver, spleen, lung, kidney, and intestine) were analyzed using H&E staining, as shown in Figure 6. Compared with the tissues of nude mice injected with PBS, fibrosis of the heart and lung was not observed, and the inflammatory reaction of the liver was also not found. Moreover, in the kidney, the glomerulus and tubules were clearly displayed, and the structure of the intestinal villus was also present in the intestine, indicating no obvious tissue lesion in histological specimens. The results suggested that the as-prepared Ag@Au-DTTC nanostars could be further applied in SERS imaging and PTT of cancers with low risk.

The *in vivo* SERS measurement of MCF-7 tumor-bearing nude mice was carried out by injecting PBS, Ag@Au, pure DTTC, and Ag@Au-DTTC nanostars, as shown in Figure 7. The Raman spectra of tumors without injection and injected with PBS, Ag@Au, and pure DTTC were similar, in which only some broad packages were appeared. However, many sharp and narrow peaks located at about 508, 782, 844, 1135, 1242, 1331, 1464, 1510, and 1580 cm^{-1} could be observed in the Raman spectrum of tumors injected with Ag@Au-DTTC nanostars. The results demonstrated that the as-prepared Ag@Au-DTTC nanostars could be promising as SERS imaging probes for *in vivo* diagnosis of cancers.

3.6. *In Vivo* PTT on MCF-7 Tumor-Bearing Nude Mice.

By establishing the MCF-7 tumor model of nude mice, the *in vivo* PTT of Ag@Au-DTTC nanostars was assessed in 14 days. The tumor-bearing nude mice were randomly divided into four groups and were injected and treated with PBS, PBS + NIR, Ag@Au-DTTC, and Ag@Au-DTTC+NIR. Figure 8a showed the change of relative tumor volume of MCF-7 tumor-bearing nude mice in 14-day treatments. At the 14th day, the relative volume of MCF-7 tumors was 5.22, 5.16, and 5.32 in groups of PBS, PBS + NIR, and Ag@Au-DTTC, respectively, but was 0.16 in the group of Ag@Au-DTTC + NIR. Moreover, the body weight of tumor-bearing nude mice in four groups did also not decrease as shown in Figure 8b. To compare the temperature change of nude mice injected with PBS and Ag@Au-DTTC nanostars under the irradiation of an 808 nm laser, the *in vivo* IR thermal imaging of MCF-7 tumors was measured. As seen in Figure 8c, the temperature of the MCF-7 tumor in the group of Ag@Au-DTTC nanostars rapidly increased under the irradiation of an 808 nm laser from 1 to 5 min. Figure 8d gave the real photograghs of MCF-7 tumor-bearing nude mice in four groups at the beginning and at the end of 14-day treatments, in which the tumor volume in the group of Ag@Au-DTTC + NIR had almost disappeared after 14-day treatments. The results demonstrated that MCF-7 tumors injected with Ag@Au-DTTC nanostars could be treated under the irradiation of an 808 nm laser.

In order to assess the risk of Ag@Au-DTTC nanostars and NIR lights for tumor treatment, the tissue sections of the tumor, heart, liver, spleen, lung, and kidney of nude mice in four groups were analyzed by H&E staining, as shown in Figure 9. For tumors, many apoptotic and necrotic tumor cells appeared in the group of Ag@Au-DTTC + NIR but not in other groups. Histological analysis of main organs revealed that pathological changes were not found in the heart, liver, spleen, lung, and kidney of different groups. The fibrosis in the heart and lung samples was not detected, and the inflammatory reaction in the liver section was also not found. Moreover, the glomerular and tubular structures in the kidney samples were clearly displayed. Therefore, it could be said that no necrosis was observed in any histological specimen except tumors. The results demonstrated the safety and the potential clinical application of Ag@Au-DTTC nanostars in improved SERS imaging and NIR-triggered PTT of breast cancers.

4. CONCLUSIONS

In summary, Ag@Au-DTTC nanostars were synthesized for *in vivo* improved SERS imaging and NIR-triggered high efficient PTT in breast cancers with good biocompatibility. Because of the coating of Au nanostars onto Ag nanoparticles, the cytotoxicity was decreased. Moreover, by two-step coupling DTTC, the SERS signal of Ag@Au-DTTC nanostars was improved by 2.63 times. The *in vitro* and *in vivo* SERS measurement demonstrated that the as-prepared Ag@Au-DTTC nanostars were excellent SERS-active enhancement agents for cells and tumors, in which sharp and narrow Raman peaks could be observed located at about 508, 1135, 1242, 1274, 1407, 1464 cm^{-1}, and so on. The as-prepared Ag@Au-DTTC nanostars showed good photostability, and the photothermal conversion efficiency was up to 79.01%. Under the irradiation of an 808 nm laser, the viability of MCF-7 cells was decreased to about 5%, and the tumor volume of the MCF-7 tumor-bearing nude mouse almost disappeared after 14-day treatments. The present work provided a critical strategy of developing theranostic nanoprobes with high performance and low toxicity, and the as-prepared Ag@Au-DTTC nanostars were valuable as a new theranostic system for simultaneously improved SERS imaging and NIR-triggered high efficient PTT in breast cancers with low risk.

■ ASSOCIATED CONTENT

Supporting Information

TEM image of Ag nanoparticles; TEM image of Ag@Au-DTTC nanostars irradiated by an 808 nm laser for 30 min; UV-vis spectra of Ag nanoparticles at different concentrations; DLS curves of Ag@Au-DTTC nanostars dispersed in deionized water, PBS, FBS, and 10% FBS during 7 days; optical microscopy and SERS mapping images of MCF-7 cells incubated with Ag@Au-DTTC nanostars; and temperature variation curves of deionized water by irradiating an 808 nm laser for 5 min with the power density of 0.4, 0.8, 1.2, 1.6, 2.0, 2.4, to 3.0 W/cm^2. The Supporting Information is available free of charge on the ACS Publications website at DOI: 10.1021/acsami.5b04548.

■ AUTHOR INFORMATION

Corresponding Authors

*(G.L.) E-mail: cjr.luguangming@vip.163.com.

DOI: 10.1021/acsami.5b04548
ACS Appl. Mater. Interfaces 2015, 7, 16781−16791

*(A.W.) E-mail: aiguo@nimte.ac.cn.

Notes

The authors declare no competing financial interest.

■ ACKNOWLEDGMENTS

This work was supported by the National Natural Science Foundation of China (U1332117, 21305148, and U1432114), the National Key Basic Research Program of China (2014CB744504), the Postdoctoral Science Foundation of China and Jiangsu Province, Science & Technology Department of Zhejiang Province (2015C31027), Science & Technology Bureau of Ningbo City (2015C50004 and 2015B11002), the Youth Innovation Promotion Association of Chinese Academy of Sciences (2015234), and Hundred Talents Program of CAS (WU A.G.).

■ REFERENCES

(1) Lee, D. E.; Koo, H.; Sun, I. C.; Ryu, J. H.; Kim, K.; Kwon, I. C. Multifunctional Nanoparticles for Multimodal Imaging and Theragnosis. *Chem. Soc. Rev.* **2012**, *41*, 2656−2672.

(2) Huang, Y.; He, S.; Cao, W.; Cai, K.; Liang, X. Biomedical Nanomaterials for Imaging-Guided Cancer Therapy. *Nanoscale* **2012**, *4*, 6135−6149.

(3) Choi, K. Y.; Liu, G.; Lee, S.; Chen, X. Y. Theranostic Nanoplatforms for Simultaneous Cancer Imaging and Therapy: Current Approaches and Future Perspectives. *Nanoscale* **2012**, *4*, 330−342.

(4) Cheng, L.; Wang, C.; Feng, L.; Yang, K.; Liu, Z. Functional Nanomaterials for Phototherapies of Cancer. *Chem. Rev.* **2014**, *114*, 10869−10939.

(5) Lim, E. K.; Kim, T.; Paik, S.; Haam, S.; Huh, Y. M.; Lee, K. Nanomaterials for Theranostics: Recent Advances and Future Challenges. *Chem. Rev.* **2015**, *115*, 327−394.

(6) Schlücker, S. Surface-Enhanced Raman Spectroscopy: Concepts and Chemical Applications. *Angew. Chem., Int. Ed.* **2014**, *53*, 4756−4795.

(7) Wang, Y.; Yan, B.; Chen, L. SERS Tags: Novel Optical Nanoprobes for Bioanalysis. *Chem. Rev.* **2013**, *113*, 1391−1428.

(8) Mulvihill, M. J.; Ling, X. Y.; Henzie, J.; Yang, P. Anisotropic Etching of Silver Nanoparticles for Plasmonic Structures Capable of Single-Particle SERS. *J. Am. Chem. Soc.* **2010**, *132*, 268−274.

(9) Lim, D. K.; Jeon, L. S.; Hwang, J. H.; Kim, H.; Kwon, S.; Suh, Y. D.; Nam, J. M. Highly Uniform and Reproducible Surface-Enhanced Raman Scattering from DNA-Tailorable Nanoparticles with 1-nm Interior Gap. *Nat. Nanotechnol.* **2011**, *6*, 452−460.

(10) Qian, J.; Jiang, L.; Cai, F.; Wang, D.; He, S. Fluorescence-Surface Enhanced Raman Scattering Co-Functionalized Gold Nanorods as Near-Infrared Probes for Purely Optical *in Vivo* Imaging. *Biomaterials* **2011**, *32*, 1601−1610.

(11) Zhang, Q.; Large, N.; Wang, H. Gold Nanoparticles with Tipped Surface Structures as Substrates for Single-Particle Surface-Enhanced Raman Spectroscopy: Concave Nanotubes, Nanotrisoctahedra, and Nanostars. *ACS Appl. Mater. Interfaces* **2014**, *6*, 17255−17267.

(12) Pradhan, M.; Chowdhury, J.; Sarkar, S.; Sinha, A. K.; Pal, T. Hierarchical Gold Flower with Sharp Tips from Controlled Galvanic Replacement Reaction for High Surface Enhanced Raman Scattering Activity. *J. Phys. Chem. C* **2012**, *116*, 24301−24313.

(13) Jokerst, J. V.; Cole, A. J.; de Sompel, D. V.; Gambhir, S. S. Detection with Photoacoustic Imaging and Resection Guidance *via* Raman Imaging in Living Mice. *ACS Nano* **2012**, *6*, 10366−10377.

(14) Song, C.; Min, L.; Zhou, N.; Yang, Y.; Su, S.; Huang, W.; Wang, L. Synthesis of Novel Gold Mesoflowers as SERS Tags for Immunoassay with Improved Sensitivity. *ACS Appl. Mater. Interfaces* **2014**, *6*, 21842−21850.

(15) Fales, A. M.; Yuan, H.; Vo-Dinh, T. Cell-Penetrating peptide Enhanced Intracellular Raman Imaging and Photodynamic Therapy. *Mol. Pharmaceutics* **2013**, *10*, 2291−2298.

(16) Schütz, M.; Steinigeweg, D.; Salehi, M.; Kömpe, K.; Schlücker, S. Hydrophilically Stabilized Gold Nanostars as SERS Labels for Tissue Imaging of the Tumor Suppressor p63 by Immuno-SERS Microscopy. *Chem. Commun.* **2011**, *47*, 4216−4218.

(17) Wang, S.; Huang, P.; Nie, L.; Xing, R.; Liu, D.; Wang, Z.; Lin, J.; Chen, S.; Niu, G.; Lu, G.; Chen, X. Single Continuous Wave Laser Induced Photodynamic/Plasmonic Photothermal Therapy Using Photosensitizer-Functionalized Gold Nanostars. *Adv. Mater.* **2013**, *25*, 3055−3061.

(18) Ayala-Orozco, C.; Urban, C.; Bishnoi, S.; Urban, A.; Charron, H.; Mitchell, T.; Shea, M.; Nanda, S.; Schiff, R.; Halas, N.; Joshi, A. Sub-100 nm Gold Nanomatryoshkas Improve Photo-Thermal Therapy Efficacy in Large and Highly Aggressive Triple Negative Breast Tumors. *J. Controlled Release* **2014**, *191*, 90−97.

(19) Vankayala, R.; Lin, C. C.; Kalluru, P.; Chiang, C. S.; Hwang, K. C. Gold Nanoshells-Mediated Bimodal Photodynamic and Photothermal Cancer Treatment Using Ultra-Low Doses of Near Infra-Red Light. *Biomaterials* **2014**, *35*, 5527−5538.

(20) Rycenga, M.; Wang, Z.; Gordon, E.; Cobley, C. M.; Schwartz, A. G.; Lo, C. S.; Xia, Y. Probing the Photothermal Effect of Gold-Based Nanocages with Surface-Enhanced Raman Scattering (SERS). *Angew. Chem., Int. Ed.* **2009**, *48*, 9924−9927.

(21) Huang, P.; Rong, P.; Lin, J.; Li, W.; Yan, X.; Zhang, M. G.; Nie, L.; Niu, G.; Lu, J.; Wang, W.; Chen, X. Triphase Interface Synthesis of Plasmonic Gold Bellflowers as Near-Infrared Light Mediated Acoustic and Thermal Theranostics. *J. Am. Chem. Soc.* **2014**, *136*, 8307−8313.

(22) Cui, Q.; Shen, G.; Yan, X.; Li, L.; Möhwald, H.; Bargheer, M. Fabrication of Au@Pt Multibranched Nanoparticles and Their Application to *in situ* SERS Monitoring. *ACS Appl. Mater. Interfaces* **2014**, *6*, 17075−17081.

(23) Yigit, M. V.; Zhu, L.; Ifediba, M. A.; Zhang, Y.; Carr, K.; Moore, A.; Medarova, Z. Noninvasive MRI-SERS Imaging in Living Mice Using an Innately Bimodal Nanomaterial. *ACS Nano* **2011**, *5*, 1056−1066.

(24) Amendola, V.; Scaramuzza, S.; Litti, L.; Meneghetti, M.; Zuccolotto, G.; Rosato, A.; Nicolato, E.; Marzola, P.; Fracasso, G.; Anselmi, C.; Pinto, M.; Colombatti, M. Magneto-Plasmonic Au-Fe Alloy Nanoparticles Designed for Multimodal SERS-MRI-CT Imaging. *Small* **2014**, *10*, 2476−2486.

(25) Zhang, W.; Wang, Y.; Sun, X.; Wang, W.; Chen, L. Mesoporous Titania Based Yolk-Shell Nanoparticles as Multifunctional Theranostic Platforms for SERS Imaging and Chemo-Photothermal Treatment. *Nanoscale* **2014**, *6*, 14514−14522.

(26) Hu, C.; Liu, Y.; Qin, J.; Nie, G.; Lei, B.; Xiao, Y.; Zheng, M.; Rong, J. Fabrication of Reduced Graphene Oxide and Silver Nanoparticle Hybrids for Raman Detection of Absorbed Folic Acid: A Potential Cancer Diagnostic Probe. *ACS Appl. Mater. Interfaces* **2013**, *5*, 4760−4768.

(27) Wang, Y.; Polavarapu, L.; Liz-marzán, L. M. Reduced Graphene Oxide-Supported Gold Nanostars forImproved SERS Sensing and Drug Delivery. *ACS Appl. Mater. Interfaces* **2014**, *6*, 21798−21805.

(28) He, R.; Wang, Y. C.; Wang, X.; Wang, Z.; Liu, G.; Zhou, W.; Wen, L.; Li, Q.; Wang, X.; Chen, X.; Zeng, J.; Hou, J. G. Facile Synthesis of Pentacle Gold-Copper Alloy Nanocrystals and Their Plasmonic and Catalytic Properties. *Nat. Commun.* **2014**, *5*, 4327 (1−10).

(29) Wijnhoven, S. W. P.; Peinenburg, W. J. G. M.; Herberts, C. A.; Hagens, W. I.; Oomen, A. G.; Heugens, E. H. W.; Roszek, B.; Bisschops, J.; Gosens, I.; de Meent, D. V.; Dekkers, S.; de Jong, W. H.; Zijverden, M. V.; Sips, A. J. A. M.; Geertsma, R. E. Nano-Silver-A Review of Available Data and Knowledge Gaps in Human and Environmental Risk Assessment. *Nanotoxicology* **2009**, *3*, 109−138.

(30) AshaRani, P. V.; Low Kah Mun, G.; Hande, M. P.; Valiyaveettil, S. Cytotoxicity and Genotoxicity of Silver Nanoparticles in Human Cells. *ACS Nano* **2009**, *3*, 279−290.

(31) Austin, L. A.; Kang, B.; Yen, C. W.; El-Sayed, M. A. Nuclear Targeted Silver Nanospheres Perturb the Cancer Cell Cycle Differently Than Those of Nanogold. *Bioconjugate Chem.* **2011**, *22*, 2324−2331.

(32) Samal, A. K.; Polavarapu, L.; Rodal-Cedeira, S.; Liz-Marzán, L. M.; Pérez-Juste, J.; Pastoriza-Santos, I. Size Tunable Au@Ag Core-Shell

DOI: 10.1021/acsami.5b04548
ACS Appl. Mater. Interfaces 2015, 7, 16781−16791

Nanoparticles: Synthesis and Surface-Enhanced Raman Scattering Properties. *Langmuir* **2013**, *29*, 15076−15082.
(33) Lee, I. H.; Lee, J. M.; Jung, Y. Controlled Protein Embedment onto Au/AgCore-Shell Nanoparticles Forimmuno-Labeling of Nano-silver Surface. *ACS Appl. Mater. Interfaces* **2014**, *6*, 7659−7664.
(34) Bai, T.; Sun, J.; Che, R.; Xu, L.; Yin, C.; Guo, Z.; Gu, N. Controllable Preparation of Core-Shell Au-Ag Nanoshuttles with Improved Refractive Index Sensitivity and SERS Activity. *ACS Appl. Mater. Interfaces* **2014**, *6*, 3331−3340.
(35) Fales, A. M.; Yuan, H.; Vo-Dinh, T. Development of Hybrid Silver-Coated Gold Nanostars for Nonaggregated Surface-Enhanced Raman Scattering. *J. Phys. Chem. C* **2014**, *118*, 3708−3715.
(36) Ma, Y.; Li, W.; Cho, E. C.; Li, Z.; Yu, T.; Zeng, J.; Xie, Z.; Xia, Y. Au@Ag Core-Shell Nanotubes With Finely Tuned and Well-Controlled Sizes, Shell Thicknesses, and Optical Properties. *ACS Nano* **2010**, *4*, 6725−6734.
(37) Patra, P. P.; Kumar, G. V. P. Single-Molecule Surface-Enhanced Raman Scattering Sensitivity of Ag-Core Au-Shell Nanoparticles: Revealed by Bi-Analyte Method. *J. Phys. Chem. Lett.* **2013**, *4*, 1167−1171.
(38) Liu, Z.; Cheng, L.; Zhang, L.; Yang, Z.; Liu, Z.; Fang, J. Sub-100 nm Hollow Au-Ag Alloy Urchin-Shaped Nanostructure with Ultrahigh Density of Nanotips for Photothermal Cancer Therapy. *Biomaterials* **2014**, *35*, 4099−4107.
(39) Jang, H.; Kim, Y. K.; Huh, H.; Min, D. H. Facile Synthesis and Intraparticle Self-Catalytic Oxidation of Dextran-Coated Hollow Au-Ag Nanoshell and Its Application for Chemo-Thermotherapy. *ACS Nano* **2014**, *8*, 467−475.
(40) Li, H.; Xia, H.; Wang, D.; Tao, X. Simple Synthesis of Monodisperse, Quasi-Spherical, Citrate-Stabilized Silver Nanocrystals in Water. *Langmuir* **2013**, *29*, 5074−5079.
(41) Liu, Y.; Ai, K.; Liu, J.; Deng, M.; He, Y.; Lu, L. Dopamine-Melanin Colloidal Nanospheres: An Efficient Near-Infrared Photothermal Therapeutic Agent for *in Vivo* Cancer Therapy. *Adv. Mater.* **2013**, *25*, 1353−1359.
(42) Zhou, J.; Lu, Z.; Zhu, X.; Wang, X.; Liao, Y.; Ma, Z.; Li, F. NIR Photothermal Therapy Using Polyaniline Nanoparticles. *Biomaterials* **2013**, *34*, 9584−9592.
(43) Zeng, J.; Goldfeld, D.; Xia, Y. A Plasmon-Assisted Optofluidic (PAOF) System for Measuring the Conversion Efficiencies of Gold Nanostructures and Controlling an Electrical Switch. *Angew. Chem., Int. Ed.* **2013**, *52*, 4169−4173.
(44) Wang, Y.; Black, K. C. L.; Luehmann, H.; Li, W.; Zhang, Y.; Cai, X.; Wan, D.; Liu, S. Y.; Li, M.; Kim, P.; Li, Z. Y.; Wang, L. V.; Liu, Y.; Xia, Y. Comparison Study of Gold Nanohexapods, Nanorods, and Nanocages for Photothermal Cancer Treatment. *ACS Nano* **2013**, *7*, 2068−2077.
(45) Tian, Q.; Tang, M.; Sun, Y.; Zou, R.; Chen, Z.; Zhu, M.; Yang, S.; Wang, J.; Wang, J.; Hu, J. Hydrophilic Flower-Like CuS Superstructures as An Efficient 980 nm Laser-Driven Photothermal Agent for Ablation of Cancer Cells. *Adv. Mater.* **2011**, *23*, 3542−3547.
(46) Yuan, H.; Khoury, C. G.; Hwang, H.; Wilson, C. M.; Grant, G. A.; Vo-Dinh, T. Gold Nanostars: Surfactant-Free Synthesis, 3D Modelling, and Two-Photon Photoluminescence Imaging. *Nanotechnology* **2012**, *23*, 075102 (1−9).
(47) Wu, H. L.; Chen, C.; Huang, M. H. Seed-Mediated Synthesis of Branched Gold Nanocrystals Derived From the Side Growth of Pentagonal Bipyramids and the Formation of Gold Nanostars. *Chem. Mater.* **2009**, *21*, 110−114.
(48) Sau, T. K.; Murphy, C. J. Room Temperature, High-Yield Synthesis of Multiple Shapes of Gold Nanoparticles in Aqueous Solution. *J. Am. Chem. Soc.* **2004**, *126*, 8648−8649.
(49) Silva, W. R.; Keller, E. L.; Frontiera, R. R. Determination of Resonance Raman Cross-Sections for Use in Biological SERS Sensing with Femtosecond Stimulated Raman Spectroscopy. *Anal. Chem.* **2014**, *86*, 7782−7787.

DOI: 10.1021/acsami.5b04548
ACS Appl. Mater. Interfaces 2015, 7, 16781−16791